



Universidad Autónoma
de Madrid

Biblos-e Archivo
Repositorio Institucional UAM

Repositorio Institucional de la Universidad Autónoma de Madrid

<https://repositorio.uam.es>

Esta es la **versión de autor** del artículo publicado en:
This is an **author produced version** of a paper published in:

Chemical Engineering Journal 428 (2022): 131128

DOI: <https://doi.org/10.1016/j.cej.2021.131128>

Copyright: © 2021 Elsevier B.V. All rights reserved.

This manuscript version is made available under the CC-BY-NC-ND 4.0
licence <http://creativecommons.org/licenses/by-nc-nd/4.0/>

El acceso a la versión del editor puede requerir la suscripción del recurso
Access to the published version may require subscription

Kinetic study of phenol hydroxylation by H₂O₂ in 3D Fe/SiC honeycomb monolithic reactors: enabling the sustainable production of dihydroxybenzenes

Gonzalo Vega^{1,*}, Asunción Quintanilla^{1,*}, Manuel Belmonte², José A. Casas¹

¹ Department of Chemical Engineering, Universidad Autónoma de Madrid, Spain

² Institute of Ceramics and Glass (ICV-CSIC), Madrid, Spain

*Corresponding authors: gonzalo.vega@uam.es (Gonzalo Vega);
asun.quintanilla@uam.es; (Asunción Quintanilla)

Abstract

The chemical kinetics of phenol hydroxylation by hydrogen peroxide (H₂O₂) to produce dihydroxybenzenes was studied using a 3D printed monolithic reactor. The monoliths were manufactured by the Robocasting technique. They consisted on honeycomb-structured Fe/SiC nanoparticles (13.5 mm in diameter and 14.8 mm in length) with triangle cell geometry and not-facing interconnected parallel channels (71 cells per cm²). The isothermal reactor was constituted by three stacked monoliths and was operated as an ideal plug flow reactor, according to the measured residence time distribution. The hydroxylation experiments were carried out at C_{PHENOL,0}= 0.33 M, phenol:H₂O₂ molar ratio 1:1, τ (space time)= 0 - 254 g h L⁻¹, T= 80, 85 and 90 °C and water as unique solvent. Experimental results showed no mass transfer limitations. The best fits were obtained for H₂O₂ decomposition with a Langmuir-Hinshelwood-Hougen-Watson kinetic model and for phenol hydroxylation, as well as, catechol and hydroquinone production, with an Eley-Rideal kinetic model. The hydroxylation reaction mechanism underlying to the developed model involved three elementary reactions: (1) adsorption of H₂O₂ molecules on the iron active sites, (2) chemical surface H₂O₂ decomposition into the hydroxyl radical

species, and (3) reaction between adsorbed radical species and phenol in solution leading to the dihydroxybenzene formation and freeing the iron catalytic active sites (*rds*).

This work contributes to the implementation of outstanding 3D Fe/SiC honeycomb monolithic reactors with a phenol selectivity above 99% at 80 °C for the sustainable production of dihydroxybenzenes.

Keywords: 3D printing; robocasting; monolithic reactor; phenol hydroxylation; dihydroxybenzenes; heterogeneous kinetic model.

1. Introduction

Dihydroxybenzene (DHBZ) production, mainly catechol (CTL) and hydroquinone (HQ), has attracted much attention over the last decades due their multiple uses in many different industrial fields, among others, the medical and pharmaceutical industry [1], agricultural chemistry [2], food industry [3] and raw materials for dyes and rubbers [4, 5].

The hydroxylation of phenol by hydrogen peroxide (H_2O_2) in presence of titanium silicalite-1 zeolite (TS-1) as catalyst is the most extended process for DHBZ production [6, 7]. Enichem company operates large capacity plants, with 10,000 tons y^{-1} , since 1986 with excellent results [8]. The TS-1 catalyst provides good DHBZ yields ($Y_{DHBZ}=18-24\%$) because the phenol conversion is high ($X_{PHENOL}=20-25\%$) and foremost the selectivity to DHBZ ($S_{DHBZ}=90-95\%$) with respect to phenol. The reaction is performed in liquid phase at mild temperatures (70-100 °C), high concentration of aqueous H_2O_2 solution (30–50 wt.%), appropriate phenol to H_2O_2 molar ratio (3-4:1) and using organic solvents (*i.e.* acetone or methanol) [5, 7]. The phenol hydroxylation over TS-1 is a diffusion-limited process, due to the micropores blocked by the adsorbed intermediate compounds and by-products, such as the undesirable tar. In fact, the TS-1 catalytic activity is lost over time [9]. For this reason, the reaction unit comprises several parallel lined reactors and a catalyst regeneration line that allows the catalyst recycling when necessary. The slurry reactors operate in batchwise. However, the process is adapted to a continuous flow operation by alternatively feeding the parallel lined reactors [9]. The catalyst regeneration line consists on its recovery by filtration and sequential washing, drying and calcination (at 550 °C) steps.

The scarce studies related to the kinetic modelling of phenol hydroxylation over TS1 catalysts have reported a Langmuir-Hinshelwood-Hougen-Watson (LHHW) type

mechanism, where the surface reaction between H_2O_2 and phenol is the rate-limiting step [10]. In contrast, when TS1 is immobilized on diatomite, the Eley-Rideal (ER) mechanism was found to be the most favourable, since the adsorption of H_2O_2 on the active sites became much stronger than that of phenol [11].

The drawbacks of the hydroxylation of phenol over TS1 catalysts are the low reaction rates due diffusional problems of the reactants, high cost of the catalyst, its reuse and the need of using organic solvents [6, 12-14]. In order to improve the sustainability, economic and environmental issues of this process, current trends are addressing the development of active and selective catalysts, *viz.* Cu supported nanoparticles [15, 16], encapsulated homogeneous catalyst such as Cu, Ni, or Zn organic complexes into zeolites [17], metal organic frameworks of Zr [5] or Fe [18], molecular sieves such as HMS [19], SBA-16 [20] and MCM-11 [21] doped with Fe or Cu, and supported enzymatic catalyst [2]; and more recently, the development of innovative catalytic reactors. Some examples of these new technologies are photocatalytic reaction systems [3, 22-24], wall microreactors [25], membrane reactors [26] and non-conventional 3D honeycomb monolithic reactors, under stirring [27] or flow operation [28].

In this line, we have manufactured 3D Fe/SiC honeycomb monoliths with interconnected channels by the Robocasting technique that enables an outstanding performance in the hydroxylation of phenol by H_2O_2 [28]. In particular, 3D Fe/SiC monoliths with triangular cell geometry and not-faced (but staggered) interconnections exhibit superior yields ($Y_{\text{DHBZ}}=29\%$) than those obtained in the commercial process with the TS-1 catalyst at 80 °C and using water as unique solvent. This yield was achieved due to the almost total selectivity to the demanding dihydroxybenzenes, $S_{\text{DHBZ}}=99.1\%$, (with a CTL to HQ molar ratio of 1.8:1) and the high phenol conversions ($X_{\text{PHENOL}}=29.6\%$) obtained under the

mentioned operated conditions. Furthermore, the activity and selectivity over the 3D Fe/SiC monoliths was maintained during 8 days without any regeneration treatment [28].

In view of these results, the motivation of our present work is to contribute to the implementation of 3D Fe/SiC inter-connected channelled monolithic reactors for the sustainable production of DHBZ. The aim is to provide an accurate kinetic model and reaction mechanism for the hydroxylation of phenol using the Fe/SiC architectures that can be simultaneously serve as chemical reactors and catalysts. Before addressing the kinetic, which encompasses the H_2O_2 consumption, phenol hydroxylation and CTL and HQ production rates, the fluid dynamic behaviour has been analysed and the mass transfer evaluated. Experimental data of concentrations for a range of spatial times and temperatures were obtained, and intrinsic kinetic rates, which best fits the data, were elucidated.

To the best of our knowledge, this is one of the first studies dealing with kinetic modelling in 3D non-conventional architecture monolithic reactors. Due to the early developmental stage of the rational design and manufacturing of tailored 3D catalytic systems [29-31], the studies recently published in this innovative field are focused, on one side, on the manufacturing technique and material characterization [32-38] and, on the other hand, on the analysis of heat and mass transfer [39-42] to demonstrate the upgrading performance of these non-conventional architectures compared to those manufactured by the conventional direct extrusion process. Therefore, our present work also contributes to the spreading of the 3D printing technology in the chemical industry.

2. Experimental

2.1 Robocast 3D Fe/SiC monoliths

1 Fe/SiC honeycomb monoliths with triangular cell geometry and interconnected channels
2 were additive manufactured by Robocasting (RoboCAD 4.0, 3-D Inks LLC). Figure 1a
3 shows the CAD patterned structure design and an image taken during the printing process.
4 The details of the Fe/SiC ink formulation and the printing process are described in
5 elsewhere [28]. The as-printed scaffolds were heat treated first at 600 °C in air for 2 h, to
6 remove the organics used in the ink formulation (*viz.* high and low molecular
7 polyethylenimine and hydroxypropyl methylcellulose), and then, at 1200 °C in argon
8 atmosphere for 5 min (pressureless spark plasma sintering furnace, SPS-510CE; Fuji
9 Electronic Industrial Co., Ltd) to enhance their mechanical robustness.

10 Real size photographs of the 3D monoliths after both thermal treatments along with the
11 cell-side view with triangular geometry and the cross-section of the interconnected
12 parallel channels are collected in Figure 1b-d. The vertical channels shows the
13 interconnections staggered located (Figure 1a and d), which provide the adequate macro-
14 porosity to the monoliths to exhibit a superior catalytic performance [28].

15 The physical properties of these monoliths are: apparent density (ρ_p) of $1.13 \text{ g}\cdot\text{cm}^{-3}$, open
16 total (ϵ_{total}) and wall (ϵ_{wall}) porosities of 0.65 and 0.33, respectively, cell density of 71
17 cells $\cdot\text{cm}^{-2}$, wall thickness (δ_{wall}) of 0.32 mm, open channel width (d_{open}) of 0.91 mm,
18 hydraulic diameter of the channel section (d_H) of 0.53 mm and channel interface area (a_v)
19 of 22.2 m^{-1} . The mass of each monolith (W) is around 1.6 g, and the specific surface area
20 (S_{BET}) is $39 \text{ m}^2\cdot\text{g}^{-1}$. Regarding to the active catalytic phase, iron silicides, *viz.* Fe_3Si and
21 $\alpha\text{-FeSi}_2$, identified by Mössbauer spectroscopy, are proposed as the iron catalytic species
22 [28].

2.2 Phenol hydroxylation

The reactor consisted of three pieces of 3D printed monoliths (total catalyst weight, W_R ~ 3.7 g, reactor diameter, D_R =13.5 mm, reactor height, H_R =44 mm, reactor volume, V_R ~ 6.3 mL, bed density, ρ_B =0.6 g·cm⁻³) stacked in a double jacket tube (GE Healthcare, XK16/20 mm), to maintain the desired reaction temperature, and settled on a small bed of spherical glass beads (3 layers of 1 mm diameter spheres), in order to assure an even flow distribution in the channels at the entrance of the monoliths. The mixture of phenol solution and H₂O₂ (30 wt.%) was preheated at the reactor temperature and fed to the bottom of the reactor at a liquid reactant flow rate (Q_L) varied from 0 to 2 mL·min⁻¹, using a piston pump (Gilson 307 HPLC). Detailed information about the operation procedure of this setup has been reported elsewhere [28].

The kinetic study was carried out at the following operating conditions: $C_{PHENOL,0}$ = 0.33 M, $C_{PHENOL,0}$: $C_{H_2O_2,0}$ = 1:1 molar, T =80-90 °C, space time ($\tau=W \cdot Q_L^{-1}$) = 0-254 g_{cat}·h·L⁻¹. Blank experiments, in the absence of catalyst, were also tested to confirm the lack of catalytic contribution to the phenol hydroxylation.

The conversion (X) of reactants (denoted by i : phenol or H₂O₂) and the phenol selectivity (S) to the identified products (j : CTL, HQ, RSL, or BQ) were calculated as follows:

$$X_i(\%) = \frac{C_{i,0} - C_{i,t}}{C_{i,0}} \cdot 100 \quad (1)$$

$$S_j(\%) = \frac{C_j}{C_{PHENOL,0} \cdot X_{PHENOL}} \cdot 100 \quad (2)$$

$$Y_j(\%) = S_j \cdot X_{PHENOL} \cdot 100 \quad (3)$$

The selectivity to the undesired product, such as tar, was calculated as:

$$S_{TAR}(\%) = 100 - \sum S_j(\%) \quad (4)$$

All the concentrations (C) are expressed on mole basis. The subscripts *o* and *t* stand for initial and a given reaction time, respectively.

2.3. Residence time distribution study

The degree of backmixing in the upflow interconnected channelled monoliths was investigated by the experimental measurement of the residence time distribution (RTD).

The same set up and monolithic reactor as the one use for the kinetic study was employed, but now with a septum placed in the liquid feed line at the entrance of the reactor. In an experiment, the system was first filled with distilled water and, then, the pump was switched off. Next, a known volume of bromophenol blue (0.5 mL), used as inert tracer, was injected into the liquid line through the septum and the pump was immediately switched to continue with the water feeding. This sequence is considered as zero time. Samples were collected at the reactor exit up to the disappearance of the dye colour. The operating conditions were: $C_{BB,0} = 0.5 \text{ g L}^{-1}$, room temperature and $Q_L = 0.5$ and 2 mL min^{-1} ($\tau = 127$ and 32 g h L^{-1} respectively).

From the resulting temporal absorbance profile of the dye tracer at the reactor exit, the outlet $E(\theta)$ curves were calculated [43, 44]:

$$E(\theta) = \frac{V_L}{Q_L} \cdot \frac{C_{BB}(t)}{\int_0^t C_{BB} dt} \quad (6)$$

where the liquid volume in the reactor (V_L) was calculated as $\varepsilon_{\text{total}} \cdot V_R$.

By fitting the $E(\theta)$ curve to the axially-dispersed plug flow model, obtained from the mass balance of the tracer injected in impulse [44]:

$$E(\theta) = \left(\frac{Pe_R}{4 \cdot \pi \cdot \theta} \right) \cdot \exp \left[-\frac{(1-\theta)^2 \cdot Pe_R}{4 \cdot \theta} \right] \quad (7)$$

it is possible to estimate the Pe_R values of the experimental reactor.

In addition to the experimental study, the Pe_R was also estimated from the axial dispersion coefficient (D_a), considering the fluid velocity ($u=Q_L / 4 \pi^{-1} D_R^{-1}$) in the channel and the reactor length ($L=H_R$):

$$Pe_R = \left(\frac{u \cdot L}{D_a} \right) \quad (8)$$

and D_a calculated by the following equation valid for laminar flow of Newtonian fluid in circular pipes [28]:

$$D_a = D_{AB} + \frac{u^2 \cdot d_t^2}{192 \cdot D_{AB}} \quad (9)$$

The first term refers to the diffusive transport of the reactants and the second one to the convective transport, both phenomena contributing to the axial dispersion [44]. The molecular diffusion coefficients (D_{AB}) for phenol and H_2O_2 in water were calculated in our previous study [45] using the Wilke-Chang correlation at different temperatures. The corresponding calculi are provided in Table S1 of the Supporting Information.

At low Pe_R numbers (< 100), the axial dispersion is mainly controlled by the convection in the channel and, then, the presence of a radial concentration profile is expected in laminar flow reactors. Meanwhile, at high Pe_R numbers (> 100), the axial dispersion is mainly controlled by the molecular diffusion and the reactor can be considered a plug-flow reactor.

2.4 Analytical methods

The progress of the reaction was followed by taking periodically liquid samples from the reactor outlet. The steady state was reached after 2-10 h, depending on the space time. Phenol and the aromatic by-products, viz. HQ, CTL, BQ and RSL, were determined by high performance liquid chromatography (Ultimate 3000, Thermo Scientific, C18 5 μm

column 150×4.6 mm, 4 mM H₂SO₄ as mobile phase, DAD detector at wavelengths of 210, 246 and 246 nm). The H₂O₂ concentration was determined by using the TiOSO₄ method in a Cary 60 Vis-UV spectrophotometer [46]. The concentration of the bromophenol blue tracer at the exit of the reactor in the RTD experiments was also measured by spectrophotometry at the wavelengths of 591 nm. Finally, the content of Fe in solution was measured by a colorimetric test with an ORBECO-Hellige-MC500 colorimeter and, in some samples confirmed by TXRF (S2 PicoFox Bruker).

2.5 Mass transfer analysis

For the investigation of the external and internal mass transfer limitation in the isothermal 3D monolithic reactor, the Carberry number (Ca) and Weisz-Parter modulus ($\eta\phi^2$) were calculated, respectively, at the reaction conditions.

The Ca number is defined as the ratio between the observed reaction rate and the maximum external mass rate:

$$Ca = \frac{(-r_i)_{obs}}{k_{i,S} a_V C_{i,b}} \quad (10)$$

The L-S mass transfer coefficient for phenol and H₂O₂ ($k_{i,S}$) were estimated by the empirical correlations proposed for microreactors ($Re < 200$) [47, 48]:

$$\begin{aligned} Sh &= 2.47 \left[1 + 0.095 \frac{d_H}{L} Re Sc \right]^{0.45} \quad \text{for } L \leq 0.05 Re Sc d_H \\ Sh &= 2.47 \quad \text{for } L > 0.05 Re Sc d_H \end{aligned} \quad (11)$$

where 2.47 is the shape factor for triangular channel geometries, and L is the reactor length.

Furthermore, the $\eta\phi^2$ moduli along the wall thickness of the channel ($\delta_{\text{wall}} = 0\text{-}0.16$ mm) were calculated as:

$$\eta\phi^2 = \frac{(-r_{i,\text{obs}}) \cdot \delta_{\text{wall}}^2}{D_{\text{eff}} C_{i,s}} \quad (12)$$

where $C_{i,s}$ is the concentration of the reactants at catalyst surface, and D_{eff} is the effective diffusion coefficients for phenol and H_2O_2 , values calculated from the molecular diffusion of each of reactant in water at a given temperature, with a tortuosity factor assumed to be 1.2 (typical for monoliths) and the $\varepsilon_{\text{wall}} = 0.33$.

The criteria used for negligible external and internal mass transfer limitation under steady-state condition stated that the Ca number must be smaller than 0.05 and $\eta\phi^2$ much below 1, respectively [43, 49].

2.6 Kinetic modelling

Assuming isothermal plug-flow through the monolith, as it will be further experimentally demonstrated, and considering the absence of reaction in the liquid phase, the mass balance of the reactant (i) can be expressed as:

$$-Q_L \cdot dC_i = (-r_i) \cdot dW \quad (13)$$

where the reaction rate of i reactant is expressed in $\text{mol}_i \text{ g}_{\text{cat}}^{-1} \text{ s}^{-1}$. Considering that Q_L remains constant, and the definition of τ , Eq. 13 can be expressed as:

$$(-r_i) = -\frac{dC_i}{d\tau} \quad (14)$$

Analogously, the reaction rate of j products (R_j), also expressed in $\text{mol g}_{\text{cat}}^{-1} \text{ s}^{-1}$, is:

$$R_j = \frac{dC_j}{d\tau} \quad (15)$$

The numerical integration of the rate equations in the plug-flow reactor with the initial conditions $C_{\text{PHENOL}} = C_{\text{PHENOL},0}$, $C_{\text{H}_2\text{O}_2} = C_{\text{H}_2\text{O}_2,0}$ and $C_{\text{CTL},0} = C_{\text{HQ},0} = C_{\text{BQ},0} = 0$ at $\tau = 0$ $\text{g}_{\text{cat}} \cdot \text{h L}^{-1}$ was solved and fitted by using the OriginLab 2017, based on the Levenberg-Marquardt algorithm for chi-square (χ^2) minimization, which is obtained by dividing the residual sum of squares (RSS) by the degrees of freedom. The model discrimination was based on statistical analysis, considering the minimum RSS value and the coefficient of determination (R^2) closer to one, and taking into account the physical meaning of the estimated parameters.

3 Results and discussion

3.1 Axial dispersion analysis

According to the Q_L used in the reactor, the range of Reynolds numbers, Re , is between 0.02 and 0.38, which means that there is a laminar flow and a parabolic velocity field all over the monolith length. With enough residence time, the radial velocity gradient-induced concentration difference can be smoothed by molecular diffusion and, then, an ideal plug-flow could be considered. To learn about this, the Pe_R was estimated by the direct fitting of the axially-dispersed plug flow model (Eq. 7) to the experimental $E(\theta)$ data, shown in Figure 2a. The estimated Pe_R values were 198 and 57 for the two flow rates performed: 0.5 and 2 mL min^{-1} , respectively. These values were similar as those obtained by the Pe_R calculated from the D_a coefficient at each Q_L by applying Eqs. 8 and 9, valid for fluids inside circular pipes. The Pe_R values at each Q_L are provided in Table S1 of the Supporting Information. As can be seen, Pe_R at room temperature was below 100 only at 2 mL min^{-1} . For calculations done at the reaction temperature of 80 °C, the

1 Pe_R values were always superior to 100 (because the diffusion coefficient increases with
2 the temperature). Therefore, it is reasonable to assume a general plug-flow behaviour in
3
4 the proposal of the reactor mass balance for the kinetic study.
5
6
7
8
9

10 11 3.2 Mass transfer evaluation 12 13

14
15 The laminar flow regime in the monolithic bed implies the absence of a boundary layer
16 over the channel surface and, therefore, the molecular diffusion is the only mechanism
17 for the external mass transfer of the reactants towards the catalytic wall (normal to the
18 flow direction). Figure 2b shows the L-S mass transfer coefficients, k_{sa_v} , estimated for
19 phenol and H_2O_2 at the three temperatures and for L equal to the length of the monolithic
20 reactor (44 mm). The calculus are detailed in Table S3a of the Supporting Information.
21
22 The condition $L > 0.05 Re Sh d_H$ was always accomplished and, then, Sh was always
23 equal to 2.47. The k_{sa_v} values were $\sim 0.22 s^{-1}$ for phenol and $\sim 0.13 s^{-1}$ for H_2O_2 , within
24 the typical values reported for monolithic reactors, 0.24-0.04 s^{-1} [50]. This difference can
25 be attributed to the favoured diffusion of phenol in water (*i.e.* $D_{PHENOL}=2.28 \cdot 10^{-5}$ while
26 $D_{H_2O_2}=1.36 \cdot 10^{-5}$ at 90 °C).
27
28
29
30
31
32
33
34
35
36
37
38
39
40
41

42 The Ca numbers also as function of $Re d_H L^{-1}$ are provided in Figure 2c (the calculus at
43 $L= 44$ mm can be found in Table S3b of the Supporting Information). The Ca number is
44 far below 0.05 for phenol and H_2O_2 at any flow rate, and even at the entrance of the
45 reactor ($Re d_H L^{-1} < 0.1$). This means that the phenol hydroxylation and the decomposition
46 of H_2O_2 on the Fe/SiC monoliths are slower than the diffusion of the reactants in the L-S
47 interphase. Thus, the external mass transfer is not rate-limiting.
48
49
50
51
52
53
54
55
56
57
58
59
60
61
62
63
64
65

Regarding to the internal diffusion of reactants across the wall thickness of the channel, the Weisz-Prater modulus ($\eta\phi^2$) was calculated at different wall channel thickness (δ_{wall} from 0 to 0.16 mm) at the different reaction temperatures according to Eq. (12). Due to the absence of external mass transfer limitations, the concentration of the reactants at the catalyst surface is equal to the concentration in the bulk (see the calculus in Table S2 of the Supporting Information). Figure 2d shows the $\eta\phi^2$ values for phenol and H_2O_2 at 80, 85 and 90 °C. All values are below 0.3, which indicates that the reaction rates for H_2O_2 decomposition and phenol hydroxylation are slower than their diffusion into the porous wall of the channels. Additionally, the values obtained for phenol are lower than the ones obtained for H_2O_2 , again, due the favoured diffusivity of the former.

3.3. Reactor performance

The results obtained in the hydroxylation reactions at different temperatures are given in Figure 3. The X_{PHENOL} and $X_{\text{H}_2\text{O}_2}$ increase with the space-time and the rise of temperature (Figure 3a). Noteworthy, the H_2O_2 decomposition is more affected by the temperature than in the case of phenol, in such a way that an increase of H_2O_2 conversion does not always resemble an increase in the phenol conversion, as can be observed at 85 and 90 °C and 254 g L^{-1} . Under these operating conditions, the X_{PHENOL} is maintained at 40%; whereas the $X_{\text{H}_2\text{O}_2}$ increases from 83 to 93%. This means that the H_2O_2 is consumed in different parallel reactions, not only in the hydroxylation of phenol. For instance, H_2O_2 can overoxidize CTL, HQ and BQ into tar at long space times [28], and it can also be decomposed into the unfruitful oxygen and water.

As can be seen in Figures 3b-d, the main products were CTL and HQ, in a molar ratio remained at around 1.8, while BQ and RSL were produced at quite low concentrations.

1 BQ behaves as an intermediate product, showing a maximum in the concentration profile
2 at low conversion, due to its equilibrium with HQ [28]. The unidentified products required
3 to close the mass balance were considered tar since none additional peaks were identified
4 by HPLC. The concentration of tar is significant at 85 and 90 °C (Figures 3b-d), which is
5 determinant for the phenol selectivity to DBHZ. The phenol hydroxylation pathway over
6 Fe/SiC can be found elsewhere [28].

14 According to this, the S_{DHBZ} is more affected by the temperature than the space time
15 (Figures 3c-d) because the reaction temperature may favour the overoxidation of DHBZ
16 to tar (more than a prolonged catalyst contact time) and likely, the adsorption of tar on
17 the catalyst surface is less favourable. For this reason, the S_{DHBZ} in the range of X_{PHENOL}
18 achieved (from 10 to 40%) remains almost constant with the temperature, being the
19 mildest one operated, at 80 °C, the most adequate for the production of DHBZ. The best
20 performance is observed at this temperature and 254 g h L^{-1} , with $S_{\text{DHBZ}} = 99.1\%$ (and
21 $Y_{\text{DHBZ}} = 29.6\%$). These results are superior to those obtained in others intensified reactors
22 such as TS-1 catalyst in a wall microreactor [25], TS-1 catalyst in a submerged membrane
23 reactor [26], FeMOF/SiC monolithic stirrer reactor [27], and also to the conventional
24 Enichem process [6, 7]. These results stand out the excellent performance of the novel
25 3D Fe/SiC honeycomb monolithic reactors with triangular cell geometries as staggered
26 interconnected channels for the sustainable production of DHBZ.

3.4. Kinetic modelling

52 The phenol hydroxylation and H_2O_2 disappearance rates were modelled considering the
53 experimental concentration vs. τ data, shown in Figures 4a-c at 70, 80 and 90 °C
54 respectively, with different kinetic models taking into account potential equations, and
55 Langmuir-Hinshelwood-Hougen-Watson (LHHW) and Eley-Rideal (ER) kinetics. The

models collected in Table 1 were the best-fit kinetic rate equations found (see Table S4 of the Supporting Information for the statistical data of each model considered). The obtained kinetic parameters at each reaction temperature are also summarized in Table 1. As expected, the H_2O_2 kinetic parameter (K), that includes the adsorption constant, decreases with the temperature; while, strikingly, the kinetic rate constants for both reactants ($k_{H_2O_2}$ and k_{PHENOL}) are not affected by the temperature. This finding suggests that each rate constant does not correspond to one elementary reaction, but they are apparent rate constants that involve a lumping of elementary reactions, as it will be further demonstrated during the elucidation of the reaction mechanisms. The validation of the apparent kinetic model for phenol and H_2O_2 can be confirmed, as Figures 4a-c illustrate, by showing the coincidence between the experimental (in symbols) and predicted (in lines) concentration profiles. Only deviations lower than 2% were obtained (see the parity plot in Figure 4d).

Regarding to the DHBZ production rates, the following considerations were taking into account:

- 1 mole of phenol produces 1 mole of CTL or HQ, therefore, it is expected that their corresponding production rates (R_j) are:

$$R_{CTL} = S_{CTL} \cdot (-r_{PHENOL}) = \frac{k_{CTL} C_{PHENOL} C_{H_2O_2}}{1 + K C_{H_2O_2}} \quad (15)$$

$$R_{HQ} = S_{HQ} \cdot (-r_{PHENOL}) = \frac{k_{HQ} C_{PHENOL} C_{H_2O_2}}{1 + K C_{H_2O_2}} \quad (16)$$

were $k_{CTL} = S_{CTL} \cdot k_{PHENOL}$ and $k_{HQ} = S_{HQ} \cdot k_{PHENOL}$, while the H_2O_2 kinetic parameter, K, keeps in the same value at each temperature (Table 1).

- BQ can be lumped with HQ since both are in redox equilibrium in the media (Figure 1) and without introducing a significant error due to the far lower production of BQ comparing to HQ (Figure 3).

The experimental and predicted concentration profiles obtained for CTL and HQ+BQ are given in Figure 4a-c, and the party plot in Figure 4d. It can be observed the good fitting of the kinetic models (Figure 4a-c) and the accuracy for predicting the experimental data (Figure 4d). The values of the estimated kinetic rate constants are collected in Table 1 and, as above mention, the k_{CTL}/k_{PHENOL} and k_{HQ+BQ}/k_{PHENOL} ratios are coincident with the experimental selectivity at each temperature (Figure 3) and, therefore, the k_{CTL}/k_{HQ+BQ} value is also around 1.8. Since the selectivity diminishes with the reaction temperature, so the k_{CTL} and k_{HQ+BQ} do (Table 1).

3.5. Reaction mechanism

According to the rate equations constituting the kinetic model (Table 1), the sustainable production of DHBZ from phenol hydroxylation by H_2O_2 with Fe/SiC monoliths takes place as follows: first, H_2O_2 decomposes into the active oxidant species (hydroxyl radicals, $HO\bullet$) on the Fe active sites (the H_2O_2 decomposition does not occur when Fe is not present in the SiC nanoparticles [45]). Besides, the H_2O_2 decomposition follows a LHHW mechanism with adsorption of H_2O_2 as the rate-controlling step, which explains the kinetic rate for H_2O_2 in Table 1. Next, the $HO\bullet$ species react with phenol molecules given rise to DHBZs. As this reaction follows an ER mechanism, see the kinetic rate equation for phenol in Table 1, the adsorbed $HO\bullet$ species hydroxylate the phenol molecules present in the liquid phase (not adsorbed). According to this, the overall chemical process can be described by the following three elementary steps:



The rate expressions of this set of reactions are:

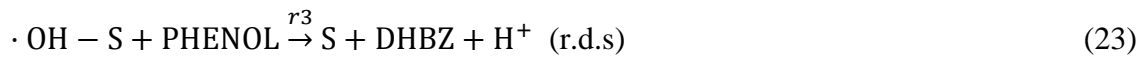
$$r_1 = k_1 C_{H_2O_2} C_S - k_{-1} C_{S-H_2O_2} \quad (20)$$

$$r_2 = k_2 C_{S-H_2O_2} - k_{-2} C_{S-HO\cdot} C_{HO^-} \quad (21)$$

$$r_3 = k_3 C_{S-HO\cdot} C_{PHENOL} - k_{-3} C_S C_{DHBZ} C_{H^+} \quad (22)$$

S , $S - H_2O_2$ and $S - HO\cdot$ represents the number of sites that are vacant, or occupied by H_2O_2 and $HO\cdot$ species, respectively. The conservation of the number of active sites leads to this site balance expression: $L = C_S + C_{S-H_2O_2} + C_{S-HO\cdot}$, where L is the total concentration of active sites.

Only by assuming as the rate determining step (*rds*) the reactive desorption reaction, Eq. (19), is possible to obtain the ER kinetic model for phenol hydroxylation (Table 1), as it is next demonstrated:



the rate can be expressed as:

$$(-r_{PHENOL}) = (r_3) = k_3 C_{S-HO\cdot} C_{PHENOL} \quad (24)$$

Besides,

$$r_1 = k_1 C_{H_2O_2} C_S - k_{-1} C_{S-H_2O_2} = 0 \quad (25)$$

$$r_2 = k_2 C_{S-H_2O_2} - k_{-2} C_{S-HO\cdot} C_{HO^-} = 0 \quad (26)$$

$$L = C_S + C_{H_2O_2-S} + C_{S-HO\cdot} \quad (27)$$

where L is the total concentration of active sites.

From Eqs. (25-27), it can be obtained the concentration of adsorbed $HO\cdot$ species:

$$C_{L-HO\cdot} = \frac{C_L k_2 C_{H_2O_2}}{\left(1 + \frac{k_{-2}}{k_2} C_{HO^-}\right) k_2 C_{H_2O_2} + \frac{k_{-1} k_{-2}}{k_1} C_{HO^-}} \quad (28)$$

and by its substitution in Eq. (24), the predicted phenol hydroxylation reaction rate results:

$$(-r_{PHENOL}) = (r_3) = \frac{\frac{k_1}{k_{-1} k_{-2}} \frac{1}{C_{HO^-}} L k_2 k_3 C_{PHENOL} C_{H_2O_2}}{1 + \left(\frac{k_1}{k_{-1} k_{-2}} \frac{1}{C_{HO^-}} + \frac{k_1}{k_2 k_{-1}}\right) k_2 C_{H_2O_2}} \quad (29)$$

It is reasonably to consider that C_{HO^-} is constant in the reaction media, since water is used as unique solvent and, obviously, also the concentration of active sites, L . Thus, the above equation can be rewritten as:

$$(-r_{PHENOL}) = \frac{k_{PHENOL} C_{PHENOL} C_{H_2O_2}}{1 + K C_{H_2O_2}} \quad (30)$$

where k_{PHENOL} and K are apparent constants that lumped ratios of constants of the three elemental steps involved (Eq. 17, 18 and 23). This can explain why k_{PHENOL} and K do not follow the Arrhenius dependence with the temperature. This rate equation (Eq. 30) is coincident with the reaction rate of phenol hydroxylation empirically obtained (Table 1). When a *rds* different from the reactive desorption reaction (Eq. 23) is assumed, then other kinetic rate equations are obtained for phenol (see Table S5 of the Supporting Information or the different assumptions) and they do not fit the experimental data. Thus, it can be concluded that the reaction mechanism proposed in Eqs. 17, 18 and 23 for the production of DHBZ from phenol hydroxylation by H_2O_2 in aqueous phase over Fe catalysts is valid.

4. Conclusions

The sustainable production of DHBZ in 3D Fe/SiC honeycomb monolithic reactors was studied by performing the hydroxylation of phenol with H_2O_2 at 80-90 °C in water as unique solvent. The discriminated kinetic model predicts the H_2O_2 consumption according to a LHHW kinetic model and phenol hydroxylation, as well as, catechol and

hydroquinone production by ER kinetic models. The robustness of the model is demonstrated by the well prediction of the concentrations of the involved species from the reaction rates of the model.

The estimated kinetic rate constants for H_2O_2 and phenol ($k_{\text{H}_2\text{O}_2}$ and k_{PHENOL} , respectively) are apparent because, though it is not a diffusion-controlled process, they lumped ratios of constants of the three elemental steps mechanistically involved: (1) H_2O_2 adsorption, (2) surface decomposition of H_2O_2 into $\text{HO}\cdot$ species and (3) reaction between adsorbed $\text{HO}\cdot$ and phenol in solution, the latter being the determining step of the hydroxylation process.

The best performances, $S_{\text{DHBZ}}=99.1$ and $Y_{\text{DHBZ}}=29.6\%$ are accomplished at the lowest reaction temperature, $80\text{ }^\circ\text{C}$, when the overoxidation of the DHBZ to tar is less favourable. Phenol is mainly oxidized to catechol ($k_{\text{CTL}}=S_{\text{CTL}}\cdot k_{\text{PHENOL}}$) and, then, to hydroquinone ($k_{\text{HQ}}=S_{\text{HQ}}\cdot k_{\text{PHENOL}}$) where the corresponding selectivity is around 60 and 33%, respectively.

The results of this study lead to a better understanding of the hydroxylation of phenol by H_2O_2 in 3D Fe/SiC honeycomb monolithic reactors and contribute to the development of an environmental friendly and cost-effective technology for the selective oxidation processes with H_2O_2 .

Acknowledgments

The authors thank the financial support by the Community of Madrid through the project S2018/EMT-4341 and the Government of Spain through the projects: PID2019-105079RB-I00, PGC2018-095642-B-I00 and RTI2018-095052-B-I00

(MCIU/AEI/FEDER, UE). Also, G. Vega acknowledges the Universidad Autonoma de Madrid for the Predoctoral contract FPI/UAM2021.

References

- [1] B. Bukowska, J. Michalowicz, A. Marczak, The effect of catechol on human peripheral blood mononuclear cells (*in vitro* study). *Environ. Toxicol. and Pharmacol.* 39 (1) (2015), 187-193. <https://doi.org/10.1016/j.etap.2014.11.017>
- [2] L. Hai, T. Zhang, S. Jiang, X. Ma, D. Wang, B. Li, Catalytic Performance and Kinetics of the Precursor of [Fe]-Hydrogenase in the Reaction of Phenol Hydroxylation in Aqueous Phase at Ambient Temperature. *Catal. Lett.* 150 (2019), 1238-1243. <https://doi.org/10.1007/s10562-019-03060-7>
- [3] S. Huixian, Z. Tianyong, L. Bin, W. Xiao, H. Meng, Q. Mingyan, Photocatalytic hydroxylation of phenol with Fe–Al-silicate photocatalyst: A clean and highly selective synthesis of dihydroxybenzenes. *Catal. Commun.* 12 (11) (2011) 1022-1026. <https://doi.org/10.1016/j.catcom.2011.03.012>
- [4] L. Hai, T. Zhang, X. Zhang, G. Zhang, B. Li, J. Shuang, X. Ma, 2017. Catalytic hydroxylation of phenol to dihydroxybenzene by Fe (II) complex in aqueous phase at ambient temperature. *Catal. Commun.* 101 (2017) 93-97. <https://doi.org/10.1016/j.catcom.2017.08.001>
- [5] B. Li, W. Wu, T. Zhang, S. Jiang, X. Chen, G. Zhang and X. Zhang, Ferrocene particles incorporated into Zr-based metal–organic frameworks for selective phenol hydroxylation to dihydroxybenzenes. *RSC Adv.*, 7 (61) (2017) 38691-38698. <https://doi.org/10.1039/C7RA06917K>

- [6] G. Centi, F. Cavani, F. Trifirò. Selective Oxidation by Heterogeneous Catalysis, first ed., Springer, New York, 2001. <https://doi.org/10.1007/978-1-4615-4175-2>
- [7] G. Bellussi, R. Millini, P. Pollesel, C. Perego, Zeolite science and technology at Eni. New J. Chem. 40 (5) (2016), 4061-4077. <https://doi.org/10.1039/C5NJ03498A>
- [8] B. Notari. Titanium Silicalite: A New Selective Oxidation Catalyst. Stud Surf Sci Catal 60 (1991) 343-352. [https://doi.org/10.1016/S0167-2991\(08\)61912-6](https://doi.org/10.1016/S0167-2991(08)61912-6)
- [9] M. G. Clerici, O. A. Kholdeeva. Liquid phase oxidation via heterogeneous catalysis. Organic Synthesis and Industrial Applications, first ed., Wiley, New Jersey, 2013. <https://doi.org/10.1002/anie.201404813>
- [10] R. Klaewkla, S. Kulprathipanja, P. Rangsunvigit, T. Rirksomboon, W. Rathbun, L. Nemeth. Kinetic modelling of phenol hydroxylation using titanium and tin silicalite-1s: Effect of tin incorporation. Chem. Eng. J. 129 (2007) 21–30 <https://doi.org/10.1016/j.cej.2006.10.034>
- [11] H. Liu, G. Lu, Y. Guo, Y. Guo, J. Wang, Chemical kinetics of hydroxylation of phenol catalyzed by TS-1/diatomite in fixed-bed reactor, Chem. Eng. J. 116 (3) (2006), 179-186. <https://doi.org/10.1016/j.cej.2005.12.001>
- [12] M. G. Clerici, O. A. Kholdeeva. Liquid phase oxidation via heterogeneous catalysis. Organic Synthesis and Industrial Applications, first ed., Wiley, New Jersey, 2013. <https://doi.org/10.1002/anie.201404813>
- [13] G. Luo, Y. Jiao, X. Lv, X. Zhang, X. Gao. Green synthesis of dihydroxybenzene from phenol with hydrogen peroxide catalyzed by iron modified FSM-16. Res. Chem. Intermed. 44 (9) (2018), 5377-5387. <https://doi.org/10.1007/s11164-018-3428-7>
- [14] H. Li, Y. Zhai, X. Zhang, G. Lv., Y. Shen, X. Wang, T. Jiang, Y. Wu, Iron-Containing TS-1 Zeolites with Controllable Mesopores by Desilication and Their

- Application in Phenol Hydroxylation. Ind. Eng. Chem. Res. 59 (22) (2020), 10289-10297. <https://doi.org/10.1021/acs.iecr.0c00048>
- [15] S. Pithakratanayothin, R. Tongsri, T. Chaisuwan, S. Wongkasemjit, A simple route to $\text{Cu}_x\text{Sn}_{(100-x)}$ intermetallic nanoparticle catalyst for ultra-phenol hydroxylation. Mater. Chem. Phys. 181 (2016) 452-461. <https://doi.org/10.1016/j.matchemphys.2016.06.081>
- [16] A. Amedlous, O. Amadine, Y. Essamlali, K. Daanoun, M. Aadil, M. Zahouily, Aqueous-phase catalytic hydroxylation of phenol with H_2O_2 by using a copper incorporated apatite nanocatalyst. RSC Adv. 9 (2019) 14132-14142. <https://doi.org/10.1039/C9RA02021GLi>
- [17] M. Maurya, Li, S. Titinchi, and S. Chand, Liquid-Phase Catalytic Hydroxylation of Phenol Using Cu (II), Ni (II) and Zn (II) Complexes of Amidate Ligand Encapsulated in Zeolite-Y as Catalysts. Catal. Lett. 89 (3-4) (2003), 219-227. <https://doi.org/10.1023/A:1025706529969>
- [18] A.D. Salazar-Aguilar, G. Vega, J.A. Casas, S.M. Vega-Díaz, F. Tristan, D. Meneses-Rodríguez, M. Belmonte, A. Quintanilla, Direct Hydroxylation of Phenol to Dihydroxybenzenes by H_2O_2 and Fe-based Metal-Organic Framework Catalyst at Room Temperature, Catal. 10 (2) (2020), 172. <https://doi.org/10.3390/catal10020172>
- [19] H. Liu, G. Lu, Y. Guo, Y. Guo, J. Wang, Study on the synthesis and the catalytic properties of Fe-HMS materials in the hydroxylation of phenol. Microporous Mesoporous Mater. 108 (1-3) (2008), 56-64. <https://doi.org/10.1016/j.micromeso.2007.03.027>
- [20] Y. Dong, X. Niu, Y. Zhu, F. Yuan, H. Fu, 2011, One-Pot Synthesis and Characterization of Cu-SBA-16 Mesoporous Molecular Sieves as an Excellent

- Catalyst for Phenol Hydroxylation. *Catal. Lett.* 141 (2) (2011), 242-250.
<https://doi.org/10.1007/s10562-010-0490-1>
- [21] Y. Jiang, K. Lin, Y. Zhang, J. Liu, G. Li, J. Sun, X. Xu, Fe-MCM-41 nanoparticles as versatile catalysts for phenol hydroxylation and for Friedel–Crafts alkylation. *Appl. Catal. B: Gen.* 445-446 (2012) 172-179. <https://doi.org/10.1016/j.apcata.2012.08.016>
- [22] K. Lv, X. Guo, X. Wu, Q. Li, W. Ho, M. Li, H. Ye, and D. Du, Photocatalytic selective oxidation of phenol to produce dihydroxybenzenes in a TiO₂/UV system: Hydroxyl radical versus hole. *Appl. Catal. B: Environ.* 199 (2016) 405-411.
<https://doi.org/10.1016/j.apcatb.2016.06.049>
- [23] B. Li, X. Chen, T. Zhang, S. Jiang, G. Zhang, W. Wu, X. Ma, Photocatalytic selective hydroxylation of phenol to dihydroxybenzene by BiOI/TiO₂ p-n heterojunction photocatalysts for enhanced photocatalytic activity. *Appl. Surf. Sci.* 439 (2018) 1047-1056. <https://doi.org/10.1016/j.apsusc.2017.12.220>
- [24] S. Gao, F. Yang, C. Song, Q. Cai, R. Wang, S. Zhou, Y. Kong, Photocatalytic producing dihydroxybenzenes from phenol enabled by gathering oxygen vacancies in ultrathin porous ZnO nanosheets. *Appl. Surf. Sci.* 505 (2020) 144580.
<https://doi.org/10.1016/j.apsusc.2019.144580>
- [25] K. Yube, M. Furuta, K. Mae. Selective oxidation of phenol with hydrogen peroxide using two types of catalytic microreactor. *Catal. Today* 125 (2007) 56-63.
<https://doi.org/10.1016/j.cattod.2007.03.017>
- [26] Ch. Lu, R. Chen, W. Xing, W. Jin, N. Xu. A submerged membrane reactor for continuous phenol hydroxylation over TS- 1. *AIChem. J.* 54 (2008).
<https://doi.org/10.1002/aic.11514>
- [27] A.D. Salazar-Aguilar, A. Quintanilla, S.M. Vega-Díaz, J.A. Casas, P. Miranzo, M.I. Osendi, M. Belmonte, Iron-based metal-organic frameworks integrated into 3D

- printed ceramic architectures, *Open Ceram.* 5 (2021) 100047.
<https://doi.org/10.1016/j.oceram.2020.100047>
- [28] G. Vega, A. Quintanilla, N. Menendez, M. Belmonte, J.A. Casas, 2021. 3D-honeycomb monoliths with interconnected channels for the sustainable production of dihydroxybenzenes: towards the intensification of selective oxidation processes. *Chem. Eng. Process. Under revision*.
- [29] C. Parra-Cabrera, C. Achille, S. Kuhn, R. Ameloot. 3D printing in chemical engineering and catalytic technology: structured catalysts, mixers and reactors, *Chem. Soc. Rev.* 47 (2018) 209-230. <https://doi.org/10.1039/c7cs00631d>.
- [30] K. M. Zentel, M. Fassbender, W. Pauer, G. A. Luinstra. Chapter Four - 3D printing as chemical reaction engineering booster. *Adv. Chem. Eng.* 56 (1) (2020) 97-137.
- [31] M. D. Symes, P. J. Kitson, J. Y. , C. J. Richmond, G. J. T. Cooper, R. W. Bowman, T. Vilbrandt, L. Cronin. Integrated 3D-printed reactionware for chemical synthesis and analysis. *Nat. Chem.* 4 (2012) 349–354. <https://doi.org/10.1038/nchem.1313>
- [32] A. Davó-Quinonero, D. Soroll-Rosario, E. Bailón-García, D. Lozano-Castelló, A. Bueno-López. Improved asymmetrical honeycomb monolith catalyst prepared using a 3D printed template, *J. Hazard. Mater.* 368 (2019) 638-643. <https://doi.org/10.1016/j.jhazmat.2019.01.092>.
- [33] F. Agueniou, H. Videl, J. de Dios López, J. C. Hernández-Garrido, M.A. Cauqui F. J botana, J. J. Calvino, V.V. Galvita, J.M. Gatica. 3D-printing of metallic honeycomb monoliths as a doorway to a new generation of catalytic devices: the Ni-based catalysts in methane dry reforming showcase. *Catal. Comm.* 148 (2021) 106181. <https://doi.org/10.1016/j.catcom.2020.106181>.
- [34] C.R. Tubío, J. Azuaje, L. Escalante, A. Coelho, F. Guitián, E. Sotelo, A. Gil. 3D printing of a heterogeneous copper-based catalyst, *J. Catal.* 334 (2016) 110–115. <https://doi.org/10.1016/j.jcat.2015.11.019>
- [35] S. Danacia, L. Protasova, F. Snijkers, W. Bouwen, A. Bengaouer, P. Marty. Innovative 3D-manufacture of structured copper supports post-coated with catalytic

- material for CO₂ methanation. Chem. Eng. Process 127 (2018) 168–177.
<https://doi.org/10.1016/j.cep.2018.03.023>
- [36] P. Michorczyk, E. Hedrzak, A. Wegrzyniak. Preparation of monolithic catalysts using 3D printed templates for oxidative coupling of methane. J. Mater. Chem. A. 4 (2016) 18753–18756. <https://doi.org/10.1039/C6TA08629B>.
- [37] S.L. Taylor, A.E. Jakus, R.N. Shah, D.C. Dunand. Iron and Nickel Cellular Structures by Sintering of 3D-Printed Oxide or Metallic Particle Inks. Adv. Eng. Mater. 19 (11) (2017) 1600365. <https://doi.org/10.1002/adem.201600365>.
- [38] J. N. Stuecker, J. E. Miller, R.E. Ferrizz, J.E. Mudd, J. Cesarano. Advanced Support Structures for Enhanced Catalytic Activity. Ind. Eng. Chem. Res. 43 (2004) 51-55. <https://doi.org/10.1021/ie030291v>
- [39] C.W.M Quinero, G. Ercolimo, A. Poozhikunnzth, R. Maric, S. Specchia. Analysis of heat and mass transfer limitations for the combustion of methane emissions on PdO/Co₃O₄ coated on ceramic open cell foams. Chem. Eng. J. 405 (2021) 126970. <https://doi.org/10.1016/j.cej.2020.126970>.
- [40] Q. Wei, H Li, G. Liu, Y. He, Y. Wang, Y. E. Tan, D. Wang, X. Peng, G. Yang, N. Tsubaki. Metal 3D printing technology for functional integration of catalytic system. Nature Communication 11 (2020) 4098-4107. <https://doi.org/10.1038/s41467-020-17941-8>
- [41] R.M. Ferriz, J. N. Stuecker, J. Cesarano, J. E. Miller. Monolithic supports with unique geometries and enhanced mass transfer. Ind. & Eng. Chem. Res. 44(2) (2005) 302-308. <https://doi.org/10.1021/ie049468r>
- [42] Y. Li, S. Chen, X. Cai, J. Hong, X. Wu, Y. Xu, J. Zou, B. H. Chen. Rational design and preparation of hierarchical monoliths through 3D printing for syngas methanation. J. Mater. Chem. A. 6 (2018) 5695-5702. <https://doi.org/10.1039/c8ta01597j>.
- [43] H. S. Fogler. Elementos de ingeniería de las reacciones químicas, fourth edition, Pearson Education, México, 2008.

- [44] O. Levenspiel. Ingeniería de las reacciones químicas, third edition, Limusa Wiley, México, 2004.
- [45] A. Quintanilla, J. A. Casas, P. Miranzo, M. I. Osendi, M. Belmonte. 3D-Printed Fe-Doped Silicon Carbide Monolithic Catalysts for Wet Peroxide Oxidation Processes. Appl. Catal. B: Environ. 235 (2018) 246-255. <https://doi.org/10.1016/j.apcatb.2018.04.066>
- [46] G.M. Eisenberg, Colorimetric determination of hydrogen peroxide, Ind. Eng.Chem. Res. Anal. Ed. 15 (1943) 327–328. <https://doi.org/10.1021/i560117a011>
- [47] N. Kockman, Heat and Mass Transfer. Transport phenomena in microprocess engineering, ed., Springer, 2008, pp. 243.
- [48] A. Renken, L. Kiwi-Misnker, Chemical Reactions in Continuous-flow Microstructured Reactors, in: N. Kockman (Ed.), Advanced Micro & Nanosystems. Volume 5. Micro Process Engineering. Fundamentals, Devices, Fabrication and Applications, Wiley, Weinheim, 2006, 173-203.
- [49] F.H.M. Dekker, A. Blik, F. Kapteijn, J.A. Moulijn, Analysis of mass and heat transfer in transient experiments over heterogeneous catalysts, Chem. Eng. Sci. 55 (22) (1995), 3573-3580. [https://doi.org/10.1016/0009-2509\(95\)00210-V](https://doi.org/10.1016/0009-2509(95)00210-V)
- [50] A. Cybulski, J. A. Moulin, Structured Catalysts and Reactors, in: J. Speight, H. Heinemann (Eds.), Chemical Industries, Taylor & Francis, Boca Raton, 2006, 359.

Table 1. Kinetic modelling for phenol hydroxylation by H₂O₂ over 3D Fe/SiC honeycomb monoliths at different temperatures

Compound	Rate equations* and kinetic parameter values		
	T= 80 °C	T= 85 °C	T= 90 °C
H₂O₂	$(-r_{H2O2}) = \frac{k_{H2O2} C_{H2O2}}{1 + K C_{H2O2}}$		
k_{H2O2} (L h ⁻¹ g _{CAT} ⁻¹)	1.7·10 ⁻² ± 3.8·10 ⁻³	1.5·10 ⁻² ± 8.3·10 ⁻³	1.5·10 ⁻² ± 2.5·10 ⁻³
K (L mol ⁻¹)	11.8 ± 3.8	8.1 ± 7.8	3.8 ± 1.9
PHENOL	$(-r_{PHENOL}) = \frac{k_{PHENOL} C_{PHENOL} C_{H2O2}}{1 + K C_{H2O2}}$		
k_{PHENOL} (L ² mol ⁻¹ h ⁻¹ g _{CAT} ⁻¹)	2.3·10 ⁻² ± 1.5·10 ⁻³	3.1·10 ⁻² ± 2.3·10 ⁻³	2.9·10 ⁻² ± 2.3·10 ⁻³
K (L mol ⁻¹)	11.8 ± 3.8	8.1 ± 7.8	3.8 ± 1.9
CATECHOL	$r_{CTL} = \frac{k_{CTL} C_{PHENOL} C_{H2O2}}{1 + K C_{H2O2}}$		
k_{CTL} (L ² mol ⁻¹ h ⁻¹ g _{CAT} ⁻¹)	1.4·10 ⁻² ± 3.8·10 ⁻⁴	1.3·10 ⁻² ± 7.8·10 ⁻⁴	1.1·10 ⁻² ± 5.2·10 ⁻⁴
K (L mol ⁻¹)	11.8 ± 3.8	8.1 ± 7.8	3.8 ± 1.9
HYDROQUINONE	$r_{HQ+BQ} = \frac{k_{HQ} C_{PHENOL} C_{H2O2}}{1 + K C_{H2O2}}$		
k_{HQ} (L ² mol ⁻¹ h ⁻¹ g _{CAT} ⁻¹)	7.8·10 ⁻³ ± 2.5·10 ⁻⁴	7.8·10 ⁻³ ± 6.1·10 ⁻⁴	5.9·10 ⁻³ ± 4.4·10 ⁻⁴
K (L mol ⁻¹)	11.8 ± 3.8	8.1 ± 7.8	3.8 ± 1.9

* Rates in mol g_{CAT}⁻¹ h⁻¹ and concentrations in mol L⁻¹

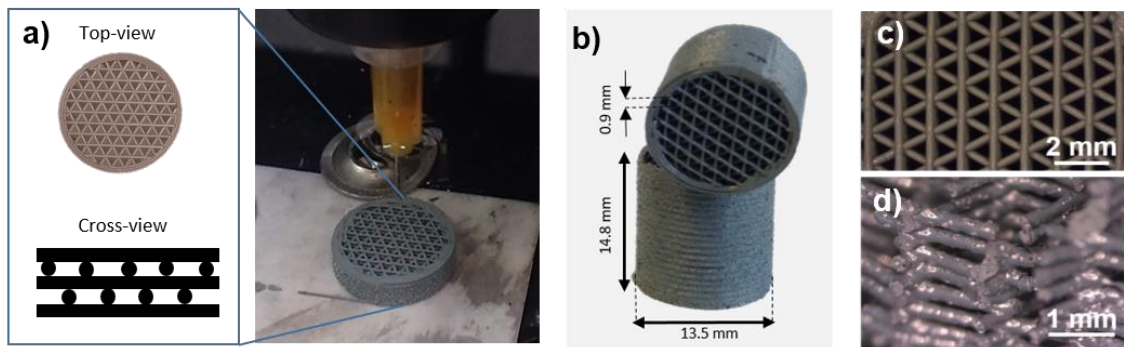


Figure 1. (a) 3D CAD design of the monolith and image of the printing process, (b) digital photograph of the top and side views of the monoliths, and (c) optical images of the cells and (d) cross-section.

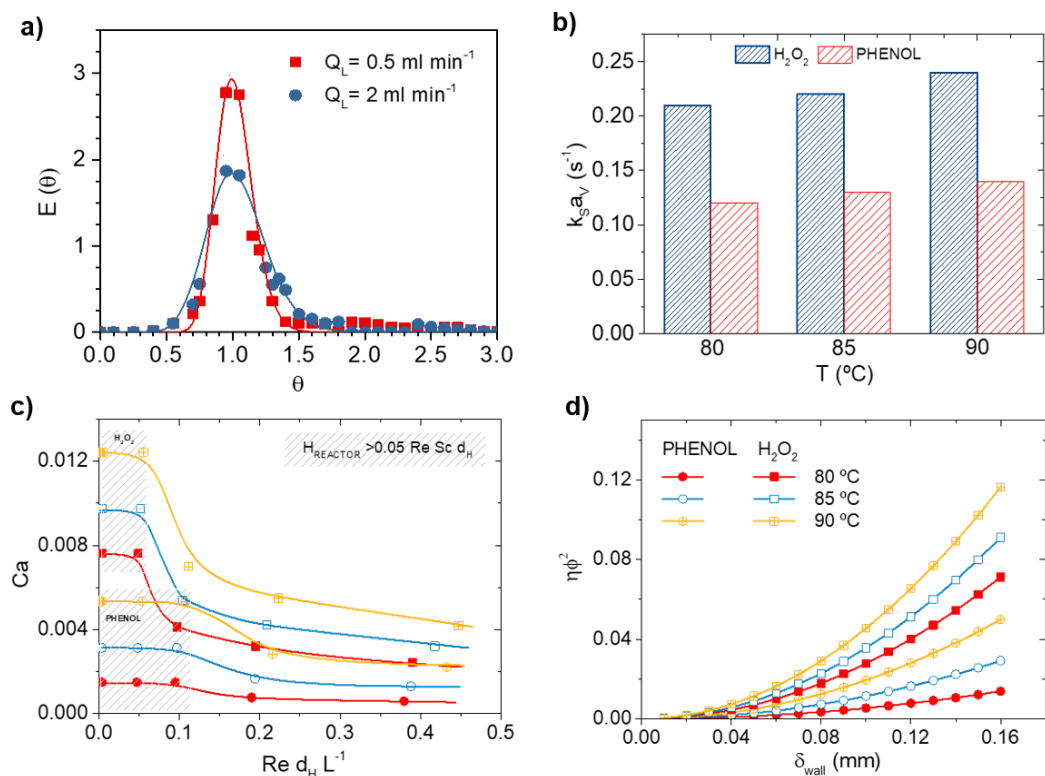


Figure 2. (a) Experimental (dotted curves) and predicted (line curve) $E(\Theta)$ curve at $Q_L = 0.5$ and 2 mL min^{-1} in the 3D monolithic reactor, (b) L-S mass transfer coefficients (k_{saV}) at $T=80-90^{\circ}\text{C}$, (c) Carberry number (Ca) with $\text{Re } d_H/L$ at $d_H = 0.53 \text{ mm}$, $L = 0-44 \text{ mm}$, $Q_L = 0.25-2 \text{ mL min}^{-1}$ and $T=80-90^{\circ}\text{C}$ (d) values of the Weisz-Prater modulus ($\eta\phi^2$) along the channel wall thickness (δ_{wall}) at $T=80-90^{\circ}\text{C}$.

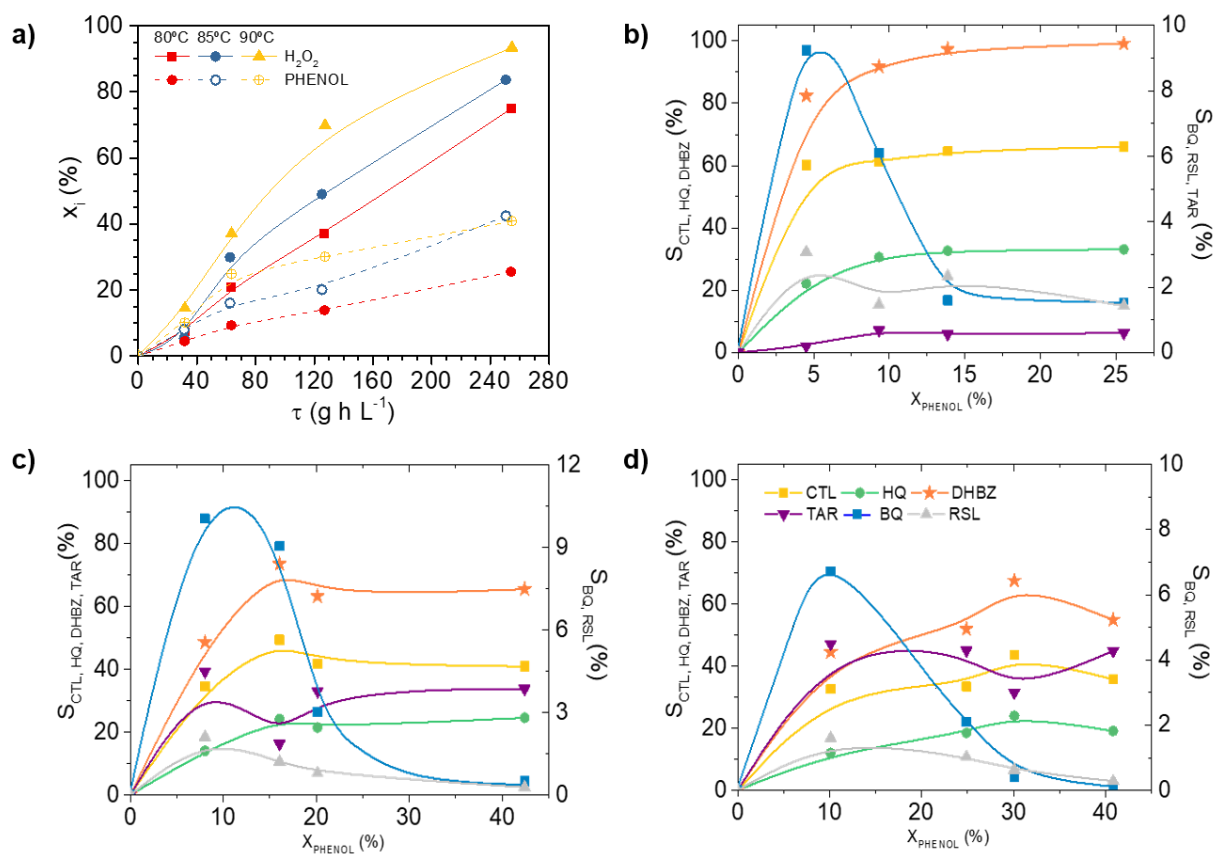


Figure 3. Results of phenol hydroxylation by H_2O_2 using 3D Fe/SiC monolithic reactors:

(a) temporal concentration profiles of H_2O_2 and phenol at different temperatures, (b) evolution of phenol selectivity at 80 °C, (c) 85 °C and (d) 90 °C.

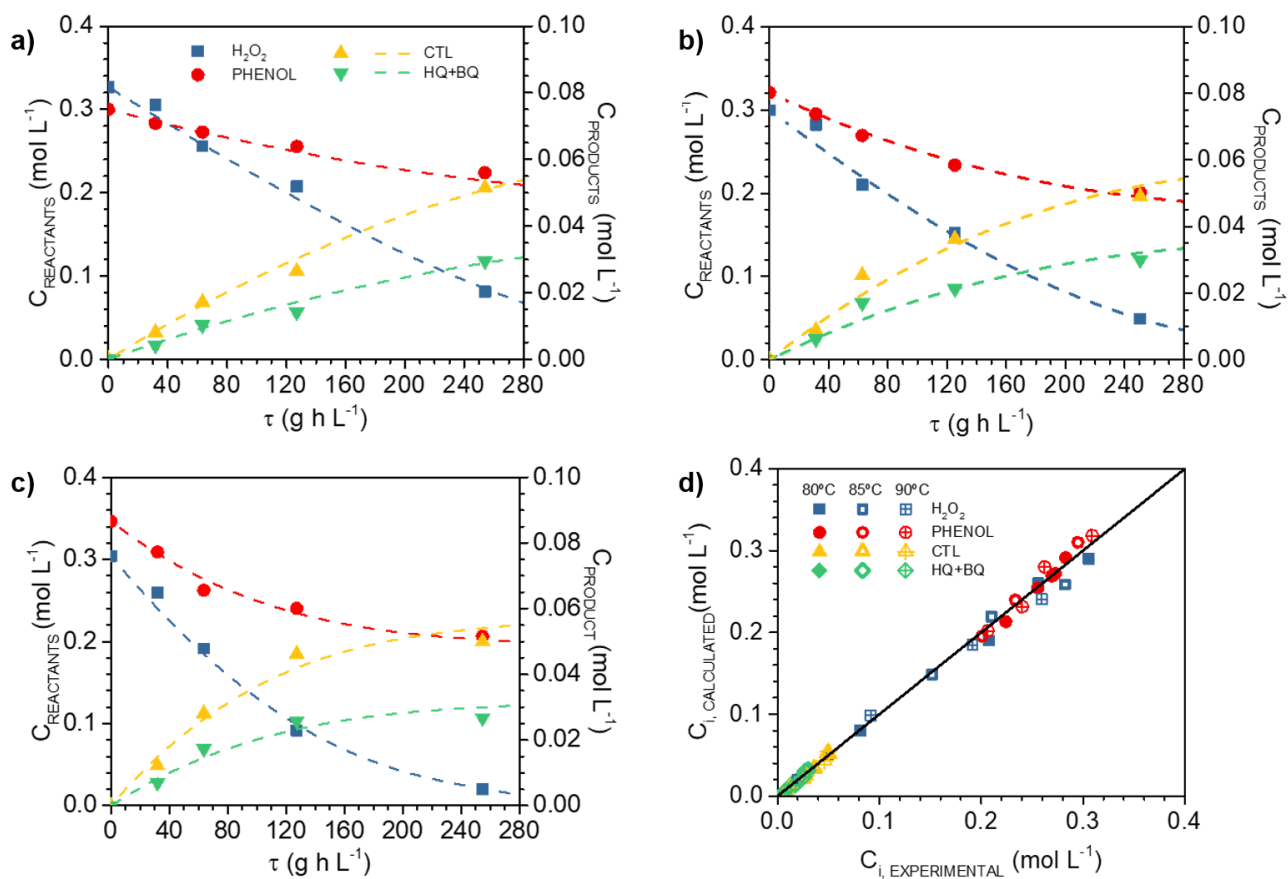


Figure 4. (a) Experimental (symbols) and predicted (curves) time-course of reactants (phenol and H_2O_2) and products (catechol and hydroquinone) at 80 °C, (b) 85 °C, (c) 90 °C and (d) parity plot of calculated and experimental concentrations at the three temperatures. Operating conditions: $C_{\text{PHENOL},0}$: $C_{\text{H}_2\text{O}_2,0} = 0.33$ M, $W_R = 3.7$ g_{CAT} and $\tau = 0$ -254 g_{cat}·h L⁻¹.